

Revealing complex optical phenomena through vectorial metrics

– Supplementary Materials –

He et al.

Supplementary Materials

Chao He^{1,*†}, Jintao Chang^{2,3,†}, Patrick S. Salter^{1,†}, Yuanxing Shen³, Ben Dai⁴, Pengcheng Li³, Yihan Jin¹, Samlan Chandran Thodika⁵, Mengmeng Li¹, Aziz Tariq⁶, Jingyu Wang¹, Jacopo Antonello¹, Yang Dong³, Ji Qi⁷, Jianyu Lin⁸, Daniel S. Elson⁸, Min Zhang⁹, Honghui He^{3,*}, Hui Ma^{2,3,*} and Martin J. Booth^{1,*}

¹*Department of Engineering Science, University of Oxford, Parks Road, Oxford, OX1 3PJ, UK*

²*Department of Physics, Tsinghua University, Beijing 100084, China*

³*Guangdong Engineering Center of Polarization Imaging and Sensing Technology, Tsinghua Shenzhen International Graduate School, Tsinghua University, Shenzhen 518055, China*

⁴*Department of Statistics, The Chinese University of Hong Kong, Shatin, HK SAR, China*

⁵*University Bordeaux, CNRS, LOMA, UMR 5798, Talence, France*

⁶*Department of Physics, Mirpur University of Science and Technology, Mirpur, AJK-10250, Pakistan*

⁷*Research Center for Intelligent Sensing, Zhejiang Lab, 310000, China*

⁸*Hamlyn Centre for Robotic Surgery, Imperial College London, London SW7 2AZ, UK*

⁹*Respiratory Department, Shenzhen Second People's Hospital, Shenzhen 518055, China*

[†]*These authors contributed equally to this work*

**Corresponding authors:*

chao.he@eng.ox.ac.uk; he.honghui@sz.tsinghua.edu.cn; mahui@tsinghua.edu.cn; martin.booth@eng.ox.ac.uk

Supplementary Material 1: Mueller matrix and the related polarisation properties.

Either a Jones matrix (JM) or a Mueller matrix (MM) can be used to describe the vectorial optical properties of an object¹⁻³. While the JM contains the information of absolute phase, it cannot represent depolarising effects of objects. The MM however can represent depolarisation, but not the overall phase¹⁻³. Hence, the MM is used if comprehensive polarisation properties need to be considered. The MM is a 4 by 4 matrix, so consists of 16 elements ($m_{kl}; k, l = 1, 2, 3, 4$). Among those elements, m_{11} represents the change in intensity, and the other 15 elements encode the vectorial properties of the object¹⁻³. The relationship between the physical quantities like retardance and these separate MM elements is often ambiguous¹⁻³.

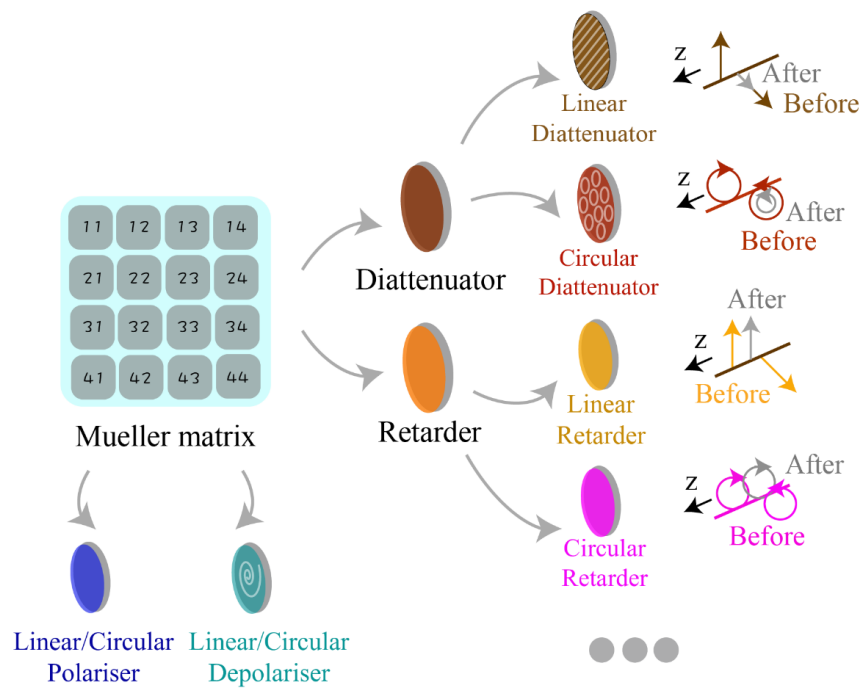
Numerous decomposition methods have been put forward⁴⁻⁶ to extract different polarisation parameters from the MM. These include linear/circular polarisation, linear/circular diattenuation, linear/circular retardance, and linear/circular depolarisation⁴⁻⁶. The various widely-used decomposition methods include: MM polar decomposition⁴, MM transformation parameters⁵, and MM anisotropic coefficients⁶. However, those approaches are based on different assumptions such as matrix reciprocity⁴, therefore they suffer intrinsic limitations in revealing the relationship to the real physical structure of a specimen – the extracted information is inherently biased to the assumed mathematical structure (some methods are shown in Supplementary Material 3). In the main article, we focus on the vectorial information decomposed from the MM that relate to the determined physical information. We refer to these quantities as “vectorial metrics”, as further detailed in Supplementary Material 2.

Supplementary Figure S1 shows a general MM and demonstrates several encoded polarisation properties. Three typical MMs are illustrated here: an arbitrary wave plate (described by parameters of retardance and axis orientation), an arbitrary polariser (described by parameters diattenuation and axis orientation), and an arbitrary depolariser (described by the parameter of depolarisation). These are shown in Ref³. For a waveplate, the parameter set $(\delta, \theta, \varepsilon)$ represents the retardance value δ , fast axis orientation θ , and the latitude parameter ε ($-\pi/2 \leq \varepsilon \leq \pi/2$) that determines the shape of the ellipse. In a polariser, the parameter set (θ, ε) encodes the transmission of a state of polarisation (SOP) with the

major axis of the ellipse oriented at θ located at latitude ε on the Poincaré sphere, where $-\pi/2 \leq \varepsilon \leq \pi/2$. In a depolariser, there exist six degrees of freedom; they are $-1 \leq a, b, c, d, e, f \leq 1$, and the corresponding MM is in a symmetric format. Note that such comprehensive polarisation properties can only be extracted via a MM (or from a JM when the medium exhibits no depolarisation), while such full properties are not accessible by other optical measurement approaches³.

$$M_{Final} = M_n \dots M_{m+1} \cdot M_m \dots M_2 \cdot M_1, \quad (1-1)$$

Eq. (1-1) models the mixed polarisation properties of a complex system M_{Final} , where the system is assumed to have n layers, and M_m represents an arbitrary layer inside such system.



Supplementary Figure S1. MM and the encoded information. There are several fundamental polarisation properties that can be extracted via the MM, such as linear/circular diattenuation, linear/circular retardance, and so on. These fundamental optical properties manipulate the light vector along propagation direction z in different format with respect to different eigenbases. They are partially demonstrated, where ‘before’ and ‘after’ illustrate the amplitude and/or phase change of the determined eigenvectors.

Supplementary Material 2: Four vectorial metrics of Mueller matrix

As we have explained in previous note, the widely adopted MM decomposition methods require different assumptions⁴⁻⁶. However, there indeed exist vectorial representations whose values are related to physical phenomena that are valid only when specific physical conditions occur (such as for certain multi-layered systems)^{3,6-9}.

We refer to such representations throughout this paper as ‘vectorial metrics’, as they reveal certain unique vectorial information. In the main article, we summarised a unified presentation of the metric Δ (first equation) to illustrate the useful quantities extracted from symmetrical or asymmetrical properties of the MM. Furthermore, we explained the how the inference network affects the scope of interpretation of Δ , which is related to information about layered structures in the specimen that can be extracted via the metrics. For instance, if we found the metric values were all zero, we would not be able to determine whether or not such a system is single-layered. As general examples of this scope, we find that certain single-layered structures can infer a zero-valued Δ , whereas the presence of certain multi-layered structures can be inferred through a non-zero value of the Δ . Note that for simplicity in this paper, we confine the scope to single layered systems that are described by a linear, rather than elliptical, eigen basis¹⁰. For similar reasons, we confine our considerations of depolarisation to homogeneous depolarisation as a single layer¹⁰. This covers the majority of realistic scenarios and does not preclude extension of the approach to more general cases in later research.

In this note, we detail the four metrics that are used in main article. Supplementary Figures S2a, S2b, S2c and S2d give an overview of the four metrics. Those metrics reveal different physical characteristics of the original complex system using asymmetric properties of the elements of the MM. Such information only exists when the system is complex, in the sense that it consists of multiple layers^{3,7-9}, as represented by Eq. (1-1). Note that theoretical studies of related parameters have been investigated before with amplification^{3,7-9}, but they have not yet been summarised into a unified structure, or been put to broad practical use. We summarise metric 1, metric 2, metric 3 and metric 4 in Eq. (2-1) to Eq. (2-4), to act as different quantitative criteria for characterizing vectorial properties in various applications.

Metric 1 is defined as

$$M_1 = m_{23} - m_{32} , \quad (2-1)$$

which relates to the asymmetry between diagonally opposed elements m_{23} and m_{32} . If this asymmetry exists, it shows that it is a multi-layered complex system that includes circular retardance⁷ (see Supplementary Figure S2a). For the GRIN lens case (a non-depolarised system) used in the main text, a non-zero M_1 gradient reflects the existence of circular birefringence gradient in a linear retarder assembly when it is obliquely illuminated. The presence of circular birefringence gradient also validates the existence of spin-Hall effect of the light in this system.

Metric 2 is defined as

$$M_2 = \sqrt{(m_{12}^2 + m_{13}^2)} - \sqrt{(m_{21}^2 + m_{31}^2)}, \quad (2-2)$$

which represents a different MM asymmetry, relating to polarisation and diattenuation. A non-zero value of M_2 indicates the presence of a multi-layered complex system that includes polarisation and diattenuation. If $M_2 > 0$, the diattenuation is stronger than polarisation in the system, and if $M_2 < 0$, the polarisation is stronger than diattenuation^{3,9}. Assuming we have ideal components, those properties determined by the sign of metric 2 can be equivalently treated as a depolariser followed by a diattenuator (or in reversed order)^{3,9} (see Supplementary Material 6). Typically, when either $\sqrt{(m_{21}^2 + m_{31}^2)}$ or $\sqrt{(m_{12}^2 + m_{13}^2)}$ equals to zero, such metric means the existence of polarisation but no diattenuation or vice versa^{3,9} (see details in Supplementary Figure S2b);

Metric 3 is defined as

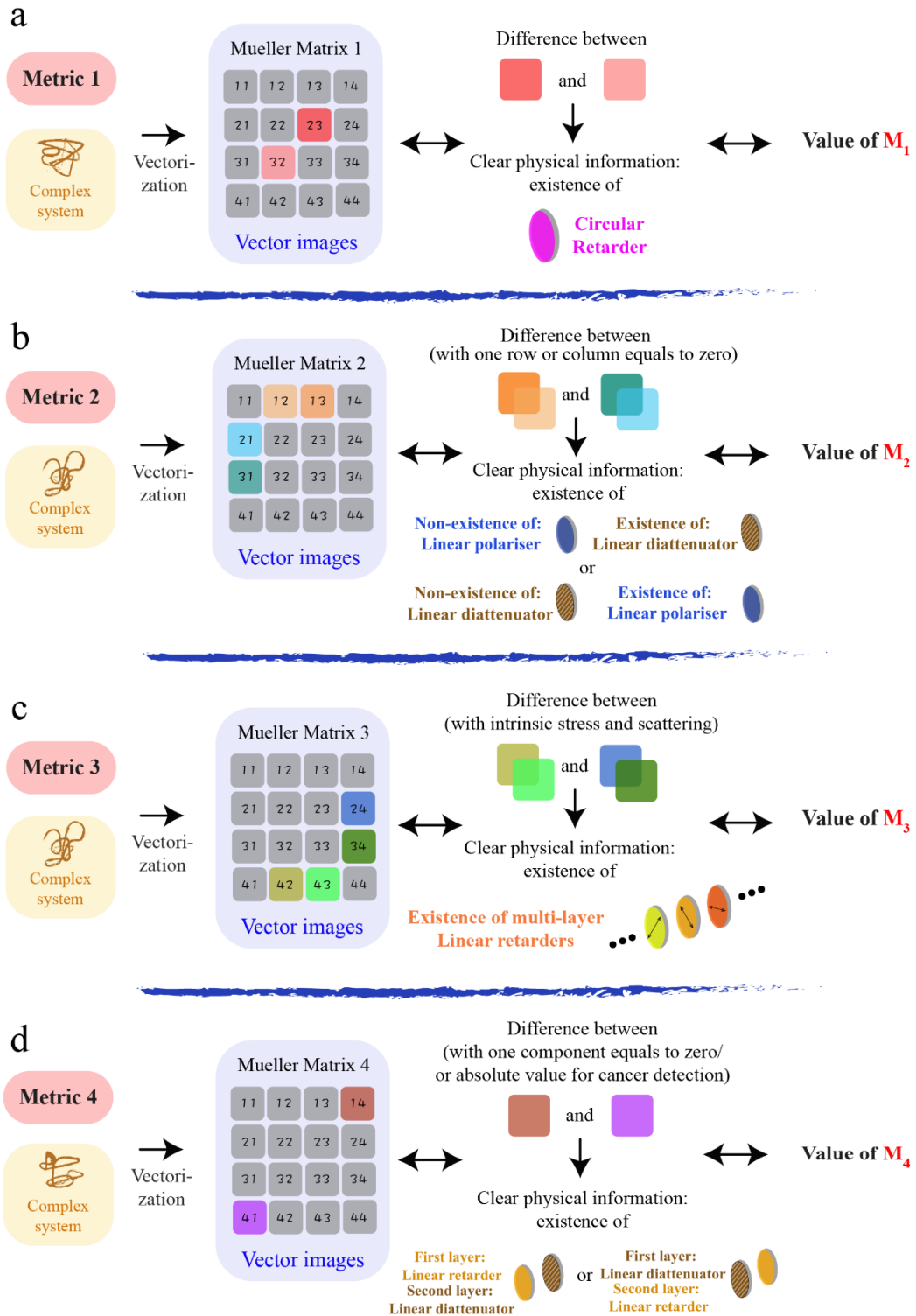
$$M_3 = \sqrt{(m_{42}^2 + m_{43}^2)} - \sqrt{(m_{24}^2 + m_{34}^2)}, \quad (2-3)$$

which represents a MM asymmetry relating to multiple retarders^{7,8}. A non-zero value of M_3 supports the presence of a multi-layered complex system that includes multi-layered retardance structure. Note in the demonstration for metric 3 throughout this paper, our analysis was based on the prior knowledge that scattering and intrinsic stress both exist in fused silica based waveguide systems. Hence, for this fabrication process specifically, this metric can act as an optimiser to balance two types of the retardance with respect to the changing writing parameters (see Supplementary Materials 5 and 9).

Metric 4 is defined as

$$M_4 = m_{14} - m_{41}, \quad (2-4)$$

which relates to the asymmetry between diagonally opposed elements m_{14} and m_{41} . A non-zero value of M_4 represents the difference between linear retardance and linear diattenuation (details see Ref⁹), which indicates the presence of a multi-layered complex system. Specifically, if $m_{41} = 0$ but $m_{14} \neq 0$, it shows a double-layered system in which the first layer is a retarder and the second layer is a diattenuator; while for $m_{41} \neq 0$ but $m_{14} = 0$, the order of layers is inverted⁷. Note such conclusions make sense under conditions when the depolarisation is negligible, such as in thin biomedical samples¹⁰⁻¹⁴.



Supplementary Figure S2. Four vectorial metrics that we used in the main article. (a) Metric 1 (M_1) focuses on the difference between element m_{23} and m_{32} , representing the existence of circular retardance. (b) Metric 2 (M_2) focuses on the difference between

$\sqrt{(m_{21}^2 + m_{31}^2)}$ and $\sqrt{(m_{12}^2 + m_{13}^2)}$, representing the relationship between polarisance and diattenuation. (c) Metric 3 (M_3) focuses on the difference between $\sqrt{(m_{42}^2 + m_{43}^2)}$ and $\sqrt{(m_{24}^2 + m_{34}^2)}$ representing the condition of multi-layered retardance. (d) Metric 4 (M_4) focuses on the difference between element m_{14} and m_{41} , representing the sequence of linear retardance and linear diattenuation.

Supplementary Material 3: Stokes-Mueller measurement and decomposed parameters of a Mueller matrix.

As the MM, its decomposed parameters and Stokes vector fields play important roles in this work, we give a brief introduction of the related measurement methods and the methods of decomposition. Supplementary Figure S3 shows a MM polarimeter using a dual-rotating wave plate method¹⁵. The polarisers (P1, P2; Thorlabs, LPVISC100-MP2) are fixed and similarly oriented. Two quarter waveplates (QWP1, QWP2; Thorlabs, AQWP10M-580) rotate with fixed rotational speeds, such that $\phi_1 = 5\phi_2$. The main measurement principle is shown in Eq. (3-1) and Eq. (3-2), where q represents the q^{th} measurement. M_{Sample} is the MM of the sample, M_{P1} , M_{P2} , M_{QWP1} and M_{QWP2} are MMs of P1, P2, QWP1 and QWP2, respectively. M_{System} is the equivalent overall MM of the system. S_{in} and S_{out} are incident and output Stokes vectors. Since the intensity is equivalent to the first element S_0 of the Stokes vector, we make $I^q = (S_{out}^q)_0$, which represents the corresponding intensity of the q^{th} measurement. From Eq. (3-2) we can obtain the Fourier series (a_n and b_n are Fourier coefficients, ϕ_1^q is the angle of QWP1 at the q^{th} measurement) and calculate the MM, detailed in Ref¹⁵.

$$S_{out}^q = M_{System}S_{in} = M_{P2}M_{QWP2}M_{QWP1}^qM_{Sample}M_{QWP1}^qM_{P1}S_{in}. \quad (3-1)$$

$$I^q = (S_{out}^q)_0 = a_0 + \sum_{n=1}^{12} [a_n \cos(2n\phi_1^q) + b_n \sin(2n\phi_1^q)]. \quad (3-2)$$

The Stokes polarimeter can be used to calculate any SOP via the sequence of recorded intensities¹⁶. As we can find in Supplementary Figure S3, the detection arm – also referred to as the polarisation state analyser (PSA) – of the MM polarimeter is a complete Stokes polarimeter. This allows measurement of the Stokes vectors of the light field by rotating the QWP2 to four different angles, following a process described in Ref¹⁶. The principal equations for calculation of field are shown in Eq. (3-3), in which S_{in} is the Stokes vector of the incident light field, M_P and M_{QWP}^n are

MMs of the corresponding polariser and waveplate, respectively. S_{out}^n is the corresponding output Stokes vector for the n^{th} fast axis orientation of QWP2. M_{QWP2}^n is the MM of QWP2 for the n^{th} fast axis orientation. A is a $n \times 4$ matrix known as the instrument matrix¹⁷⁻²⁰, which is derived from $M_P \cdot M_{QWP2}^n$. I is the intensity information recorded by the camera. More practical derivations can be found in Ref¹⁷⁻²⁰.

$$S_{out}^n = M_P M_{QWP2}^n S_{in}, \quad (n = 1, 2, 3, 4 \dots)$$

$$I = A \cdot S_{in}, \quad (3-3)$$

$$S_{in} = A^{-1} \cdot I.$$

As we mentioned, a MM contains 16 elements, but the relationship between physical quantities and these individual elements is often ambiguous. Previous research has concerned the extraction of specific polarisation parameters from the MM to characterize the optical properties of the object. We introduce two widely used MM decomposition methods in this Note, and use different sub-set of them throughout this work. Even they are limited via different assumptions^{4,6}, they can still be candidates for assessment of the performance of our metrics. For instance, in the section on biomedical analysis, we use retardance to compare and validate the performance of M_4 (see Supplementary Material 7).

One prevalent method is the MM polar-decomposition (MMPD) proposed by *Lu* and *Chipman*⁴, which has been widely used and validated for characterization of biomedical and material samples. In the main article, we specifically use the retardance parameter (R), which is suitable for analyzing complex turbid biomedical tissue; this has been applied previously in quantitative biological diagnosis¹¹⁻¹⁴. The principle of MMPD is represented by Eq. (3-4), where M_Δ , M_R and M_D are the 4×4 sub-matrices of depolarisation, retardance, and diattenuation, respectively.

$$M_{Sample} = M_\Delta M_R M_D. \quad (3-4)$$

The retardance R is reconstructed from the trace of M_R ; while the orientation of optical axis of linear retardance θ (with respect to the horizontal axis) ranging from $-\frac{\pi}{2}$ to $\frac{\pi}{2}$ radians are calculated using Eq. (3-5). The diattenuation value D can be readily obtained from the second to the fourth elements in the first row of a MM, while depolarisation properties are included in the bottom right 3×3 matrix m_Δ of the matrix M_Δ , in which λ_1, λ_2 and λ_3 are the eigenvalues of m_Δ , and P is a matrix composed of the eigenvectors of m_Δ .

$$R = \cos^{-1} \left[\frac{\text{tr}(M_R)}{2} - 1 \right],$$

$$\theta = \frac{1}{2} \tan^{-1} \left[\frac{M_{R23} - M_{R32}}{M_{R31} - M_{R13}} \right],$$

(3-5)

$$D = \sqrt{m_{12}^2 + m_{13}^2 + m_{14}^2},$$

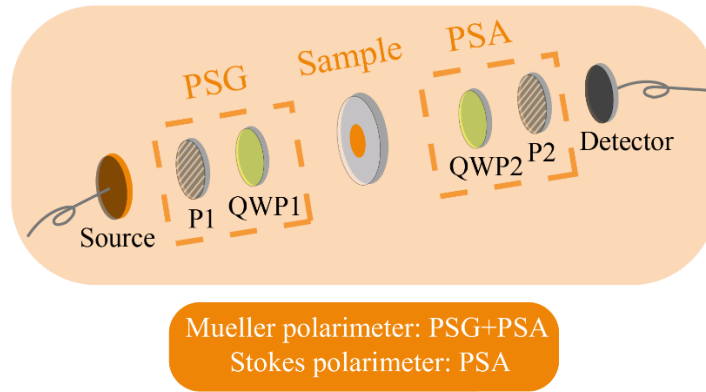
$$m_\Delta = P \begin{pmatrix} \lambda_1 & 0 & 0 \\ 0 & \lambda_2 & 0 \\ 0 & 0 & \lambda_3 \end{pmatrix} P^{-1}.$$

Arteaga et al. derived MM anisotropy coefficients (MMAC) to describe the degree of different kinds of anisotropy that might be present⁶. Intuitively, the parameters α , β , and γ from MMAC can be regarded as ratios of horizontal linear anisotropy, 45° linear anisotropy and circular anisotropy respectively with respect to the global anisotropy of the MM⁶. Among them, the circular parameter γ is used to directly reflect the existence of circular retardance, which is also used as an example to determine the existence of spin-Hall effect of light (SHEL)²¹. We use γ to validate the SHEL in a GRIN lens system as supporting evidence for using M_1 . The mathematical definition of the parameter γ with respect to MM elements is shown in Eq. (3-6). For a specific system, if the relative sign between dichroism and birefringence is known, the sign of the MMAC parameters γ can be determined as well. Details can be found in Ref⁶.

$$\Sigma = 3m_{11}^2 - (m_{22}^2 + m_{33}^2 + m_{44}^2) + 2\Delta,$$

$$\gamma = \sqrt{\frac{1}{\Sigma}[(m_{14} + m_{41})^2 + (m_{23} - m_{32})^2]}, \quad (3-6)$$

$$\text{sign}(\gamma) = \text{sign}(m_{14} + m_{41} \mp (m_{23} - m_{32})).$$



Supplementary Figure S3. Schematic construction of the MM/Stokes polarimeter. P1, P2: fixed polariser; QWP1, QWP2: rotating quarter waveplate; a camera is used as the detector. Polarisation state generator (PSG) and polarisation state analyser (PSA) are shown in dotted boxes.

Supplementary Material 4: Topological charge transfer analysis – from the point of view of angular momentum conservation

It is widely appreciated that in a rotationally symmetric system, the spin orbital interaction (SOI) results in spin-orbital angular momentum conversion (SOC), which normally generates vortex beams²². In a system with broken symmetry, the SOI process leads to the spin-Hall effect of light (SHEL), which is directly related to the occurrence of circular birefringence (CB) gradient^{21,23}. A GRIN lens has a spatially variant linear birefringence whose fast axis has an azimuthal distribution. It can be treated as a spatially variant waveplate array^{18,19,24}. In this work, we break the symmetry of the polarisation aberration of a GRIN lens system by applying collimated, oblique illumination, which experiences a different birefringence to an on-axis beam. Within the numerical aperture (NA) of the GRIN lens, the level of SHEL is determined by the incident angle.

There are various methods to validate the SHEL, such as standard quantum weak measurement methods, Stokes vector analysis, or MM analysis^{21,23,25}. The previous two are not suitable for the validation of weak SHEL with complex polarisation modulation, which can be induced by complex Pancharatnam-Berry (PB) phase gradient across the beam transverse plane. Hence, the MM and its decomposition parameters provide unique advantages²¹. They have been used previously for mapping the complex topological structures of the fast-axis orientation of various crystals and validating the appearance of SHEL^{21,24}.

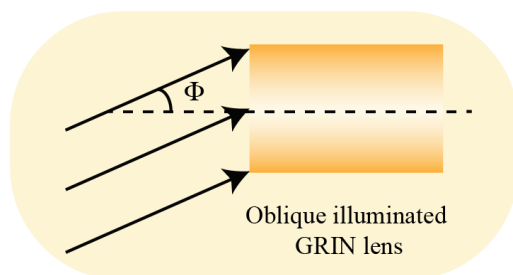
Here, we demonstrate the SHEL through illuminating a long GRIN lens (Femto Technology Co. Ltd., NA=0.25, 184mm) via an oblique incident angle. Supplementary Figure S4 shows the experimental sketch; the incident angle Φ is between 5° and 10° , with a 1° increment. We measure the full polarisation properties of the GRIN lens through obtaining different MMs for different illumination angles. We then calculate the MMPD and MMAC parameters to analyse the intrinsic mechanism of the related SOI processes. This procedure also acts to validate feasibility for the usage of M_1 for identification of SHEL. Figure S5 shows the results of different MMs (see Supplementary Figure S5a), different retardance values (see Supplementary Figure S5b) and spatially variant fast axis distributions (see Supplementary Figure

S5c), which are derived from the measured MMs. Note when a tilt is applied, the rotational symmetry of the birefringence distribution is broken (manifested in Supplementary Figures S5b and S5c).

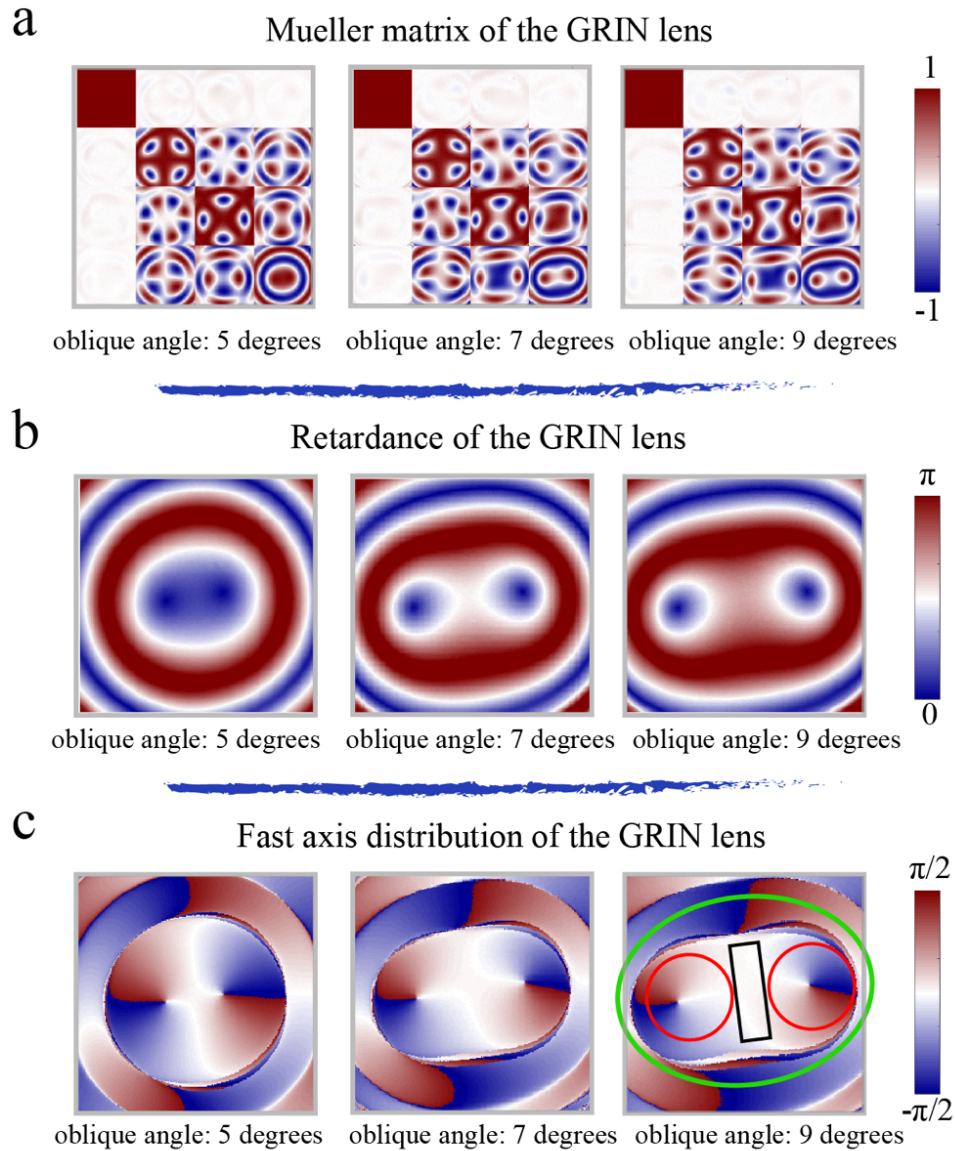
The SOI process can be understood from the point of view of angular momentum (AM) conversion. In any complex SOI process in crystals, several topological patterns holding different topological charges are used to assist the descriptions of their AM conversion process – such patterns include the lemon, star, spiral, and node²¹. Suppose we have a right hand polarised photon that carries total AM (TAM) $J = +1\hbar$, consisting of spin angular momentum (SAM) $\sigma = +1\hbar$ and OAM $l = 0\hbar$. When it passes a GRIN lens, the interaction in the node topological area in Supplementary Figure S5c converts SAM handedness of the photon into $\sigma = -1\hbar$. The TAM is changed by a SAM induced factor $+2\hbar$, where the SAM completely transfers to an intrinsic OAM (IOAM). This would significantly change the SOI process, since there exist three different topologies rather than a pure node topological pattern. From Supplementary Figure S5c (when the incident angle is 9°) we could clearly find two lemons (red circles), a node (green ellipse), and one linear gradient (black rectangle) at the intermediate region. For the node region, the SOC performance is discussed above. For the lemon regions (which are newly formed), they would gain an IOAM of $+1\hbar$. So, considering the whole field, due to the TAM conservation mechanism, the remaining $+1\hbar$ is expected to transfer into the medium – which is also comparable with the SOI process in KDP²¹. The linear gradient areas (black rectangle) are not associated with any azimuthal/radial coordinate. For such a beam-field, the photons passing through this region would neither obtain IOAM nor involve any SOC. Hence, from the point of view of AM conservation, such a region could contribute to extrinsic OAM hence validating the existence of SHEL.

The level of SHEL is quantified via γ at different illumination angles. The process is as follows: 1) we chose three fixed concentric circles on the GRIN lens surface (shown in Supplementary Figure S6a with dotted rectangles) near the linear gradient region; 2) at every angle, we obtained the data from the absolute value of γ of the three rectangles; 3) we calculated the mean value and standard deviation through statistical methods²⁶; 4) we collected data from different angles and formed the Supplementary Table S1 and Figure S6b, which show that γ increases with incident angle. To the best of our knowledge, this is the first report of SHEL in a GRIN lens system, as revealed via MM analysis. As the

GRIN lens still maintains its basic function as an imaging lens, there exists potential that the GRIN lens can combine imaging and SHEL detection.



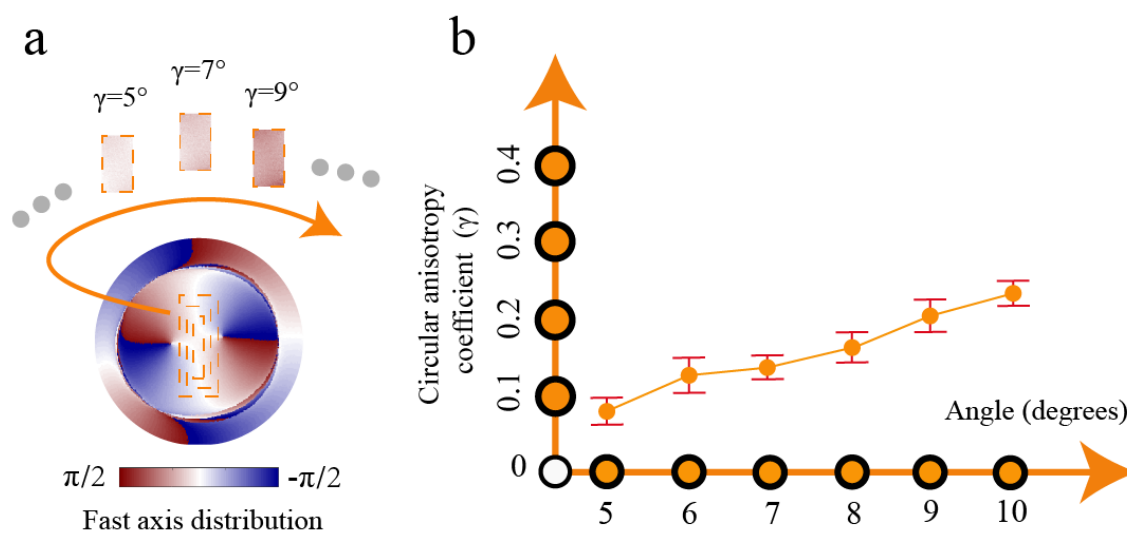
Supplementary Figure S4. Sketch of GRIN lens oblique illuminated by collimated light beam. The incident angle Φ was varied between 5° and 10° as MMs were recorded.



Supplementary Figure S5. Experimental results of MM and decomposed parameters under different illumination angles. (a) MMs of GRIN lens with different angle; (b) retardance properties of the GRIN lens; (c) fast axis properties of the GRIN lens. They are demonstrated at incident angle Φ of 5° , 7° and 9° . The green circle, red circle and black box rectangle represent different topological charge units.

Supplementary Table S1. Circular anisotropy coefficient (γ) value under different illumination angles

	5°	6°	7°	8°	9°	10°
Mean value	0.083	0.128	0.133	0.166	0.209	0.234
Standard derivation	0.021	0.026	0.018	0.024	0.025	0.019



Supplementary Figure S6. Parameter γ extracted from the measured MMs. Value of parameter γ extracted under different illumination angles. (a) The three fixed rectangle regions chosen from same physical locations on GRIN lens surface for γ value estimation for each determined illumination angle. (b) The solid yellow circle points and the red error bars represent the mean values and the standard deviation of the γ of three rectangles that were measured at every illumination angle.

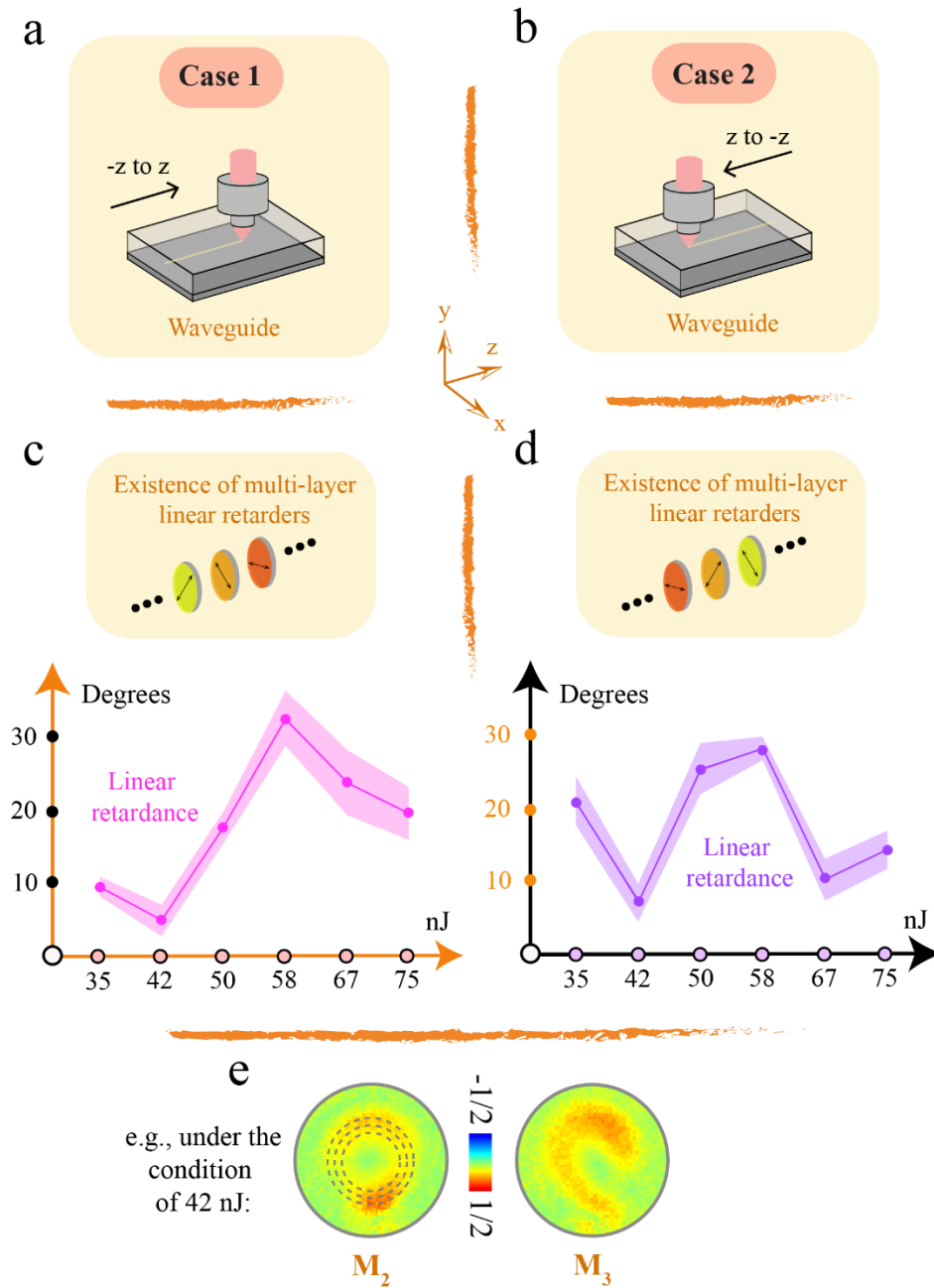
Supplementary Material 5: Direct laser writing of photonic waveguides

Direct laser writing was used to manufacture the photonic waveguides that were studied through metric 2 in the main article. The waveguides were written inside fused silica (Schott Lithosil Q0) with a tightly focused ultrashort pulse laser (Yb:KGW laser, Light Conversion Pharos SP-06-1000-pp; 1 MHz repetition rate; 514 nm wavelength; 170 fs pulse duration). The laser was focused 300 μm below the top surface of the glass with a 0.5 NA objective lens, and its power was controlled by a rotating half waveplate in conjunction with a polarisation beam splitter (PBS). A liquid crystal spatial light modulator was used to compensate system and sample aberrations encountered during processing, as described in Ref^{27,28}. The fused silica chip was mounted on a 3-axis precision translation stage (Aerotech ABL10100L/ABL10100L/ANT95-3-V). Waveguides were written by scanning transverse to the optic axis at a speed of 2 mm/s. The writing pulse energy was measured *in situ* at the sample plane, with six values of 35nJ, 42nJ, 50nJ, 58nJ, 67nJ, 75nJ, which were used in the analysis in the main article.

In case 2 in the main article, the value of M_3 indicated the existence of a multi-layered linear retarder assembly. It is known that retardance is induced here through scattering and intrinsic stress, so the information we extract is only indicative of average waveguide performance. However, such an approach also presents new possibilities for an optimized fabrication process; e.g., if the value of M_3 vanishes through changing the writing parameters, it may prove to be suitable for feedback control, showing an overall retardance performance inside the complex waveguide. In polarisation optics, matrix reciprocity always exists in a multiply layered system, and hence leads to different polarimetric properties observations when flipping the specimen¹⁻³. Since the asymmetric MM elements were observed in main article for waveguides under the above writing parameters, we also wrote identical waveguides bi-directionally to test this hypothesis (see details in Supplementary Figure S7a). The linear retardance value of those waveguides was decomposed and is shown in Supplementary Figures S7b and S7c for the six different pulse energies. The results are symptomatic of the quill effect^{29,30}, where the laser induced structural modification inside an isotropic material is different when reversing the writing direction. Here we additionally confirm the directionality in the fabrication from a polarisation optics standpoint (compared with existing methods^{29,30}) using the different small retardance values that are

provided via MM images. The same laser writing parameters lead to different linear retardance for opposite writing directions. The statistical estimation approach is shown in Supplementary Figure S7e; we chose three fixed circle regions within the aperture (shown in dotted circles, data collected within the circular 2D regions) for statistical approach refer to Ref²⁶. Note the waveguides were written in opposite directions but measured in the same orientation; the sample orientation was also flipped in testing for the quill effect.

To the best of our knowledge, it is the first time that the quill effect (and the corresponding trends) in direct laser written waveguides has been investigated from the point of view of the asymmetric information and decomposed polarisation parameters from the MMs. Note here that we used MMPD methods to extract the linear retardance simply for validation and comparison, but bear in mind the complex intrinsic isotropic/anisotropic scattering-induced vectorial manipulation for the beams are still to be explored – as it would affect the intensity loss and polarisation independence as well, in conjunction with the effects from the stress induced retarders. There is intriguing scope for future work.



Supplementary Figure S7. Two direct laser writing cases with different writing directions. (a) and (b), sketches for the two cases. (c) and (d) the measured linear retardance for the two direction cases with different writing powers. (e) Regions chosen for statistical analysis (data within three fixed dotted circles were used in the plot of the value of various polarisation properties for illustration). Taking retardance as an example, as in (c), the mean value of the dataset is shown by the solid pink circle points, while the transparent pink regions represent the standard deviations.

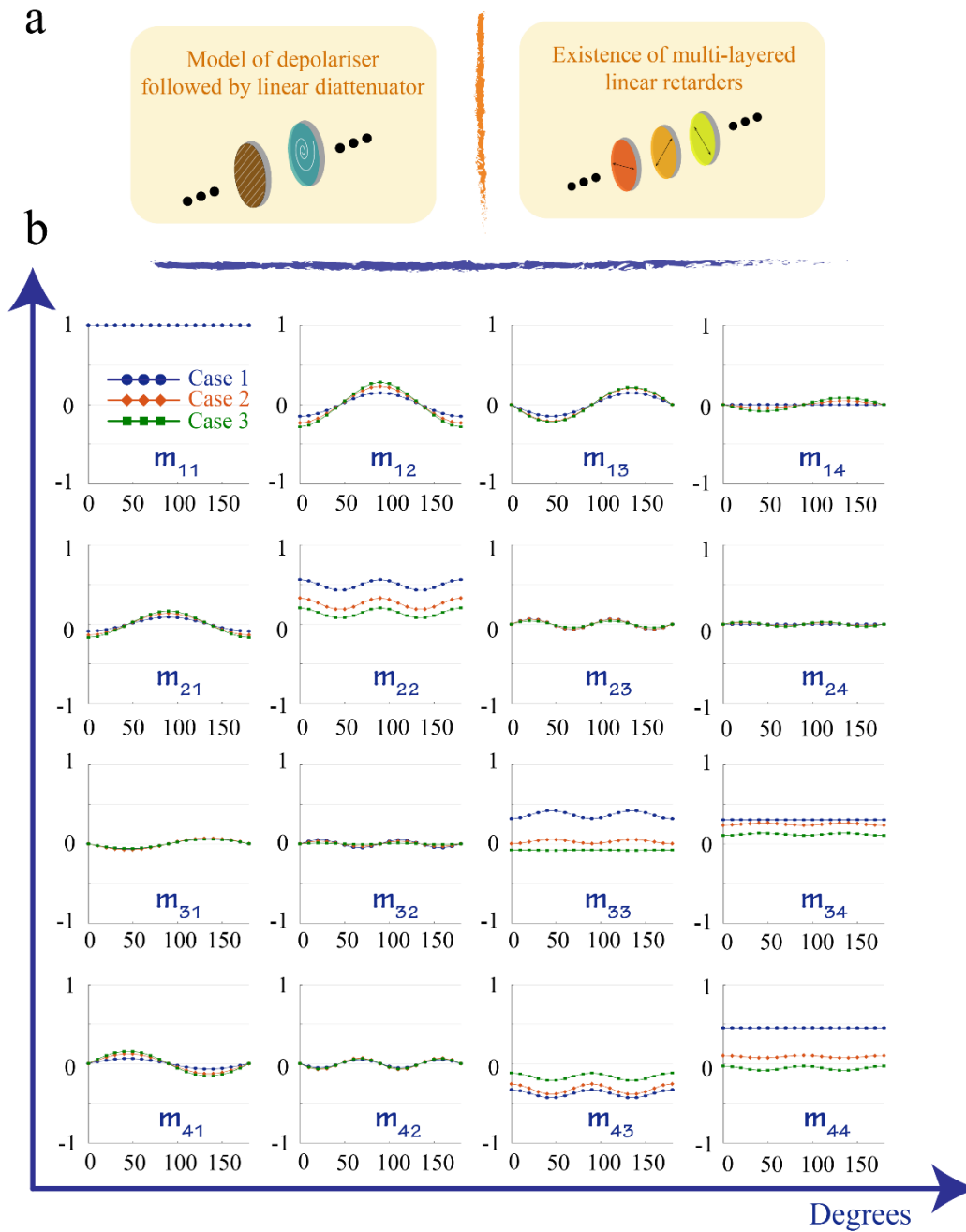
Supplementary Material 6: Monte Carlo simulation of intrinsic waveguide optical processes

The waveguides were written in fused silica, which has no inherent polarisation properties. Hence, the polarisation modulations that were observed are due to material changes induced by the direct laser writing process³⁰⁻³². Previous studies have validated that nano-structures³³⁻³⁹ can be formed in such processes inside fused silica, and that the optical properties change with laser pulse energy (and other parameters), as does the related scattering. Considering that anisotropic scattering and the isotropic scattering both exist in the waveguides, for a better understanding of the experimental results, we carried out Monte Carlo (MC) simulation^{10,40,41} with a sphere-cylinder birefringence model (SCBM) to simulate the interactions between polarised photons and the nano-structures of the waveguide. In the SCBM model, the spherical and infinitely long cylindrical scatterers can provide isotropic and anisotropic scattering effects, respectively. Previous studies have also indicated that the anisotropic scatterers can generate linear diattenuation (anisotropic absorption)¹⁰, which can be extracted quantitatively using MM elements. To study the propagation of polarised light in a waveguide, during the MC simulations the scattering coefficients, refractive indices, sizes of both scatterers, the orientation and angular distribution of the cylindrical scatterers, together with the value and fast axis orientation of birefringence for interstitial medium can all be adjusted. Here in this study, the following simulation parameters were used: a two-layered medium (case 1 in Supplementary Figure S8), four-layered medium (case 2), six-layered medium (case 3); case 2 and case 3 have periodic double-layered medium in case 1, which fit the periodic structure that occurs inside the waveguides³⁵⁻³⁷. The thickness of overall layer was 13.6 μm to match the fused silica sample that was used in the experiment. In each double-layered structure: layer 1 consisted of well-ordered cylindrical scatterers with scattering coefficient and size 1 cm^{-1} and $0.01\text{ }\mu\text{m}$, respectively; the cylinders were distributed along the X axis direction with 5° fluctuations. Layer 2 consisted of spheres and birefringent interstitial medium, the scattering coefficient and size were 15 cm^{-1} and $0.3\text{ }\mu\text{m}$, respectively; the value and fast axis orientation of birefringence were set to be $\Delta n=0.002$ and 0° , respectively.

Supplementary Figure S8 shows the MC simulated results, which contain polarisation as well as diattenuation and retardance. Such phenomena can also be explained via a layered structure model: scattering-induced depolarisation,

followed with a scattering-induced diattenuator, see Supplementary Figure S8a. From the simulated results shown in Supplementary Figure S8b, we can observe that with the direction of cylinders changes from 0° to 180° . For each case, the value fluctuations of m_{12} and m_{13} are more prominent than those of m_{21} and m_{31} , indicating that diattenuation is more dominant than polarisation for these cases. Meanwhile, the values of m_{42} and m_{43} are also larger than those of m_{24} and m_{34} , showing the existence of layered linear retardance. Supplementary Figure S8b demonstrates different numbers of the layered structures consisting of the units shown in Supplementary Figure S8a, which mimics the periodic structure that occurs inside the waveguides, as mentioned before.

The MC simulation built a link between the measured data of the waveguides as well as the possible polarisation properties models. Given the amplitudes and trends of the elements in M_2 and M_3 using MC simulation, we also validated the usefulness of our vectorial metrics.



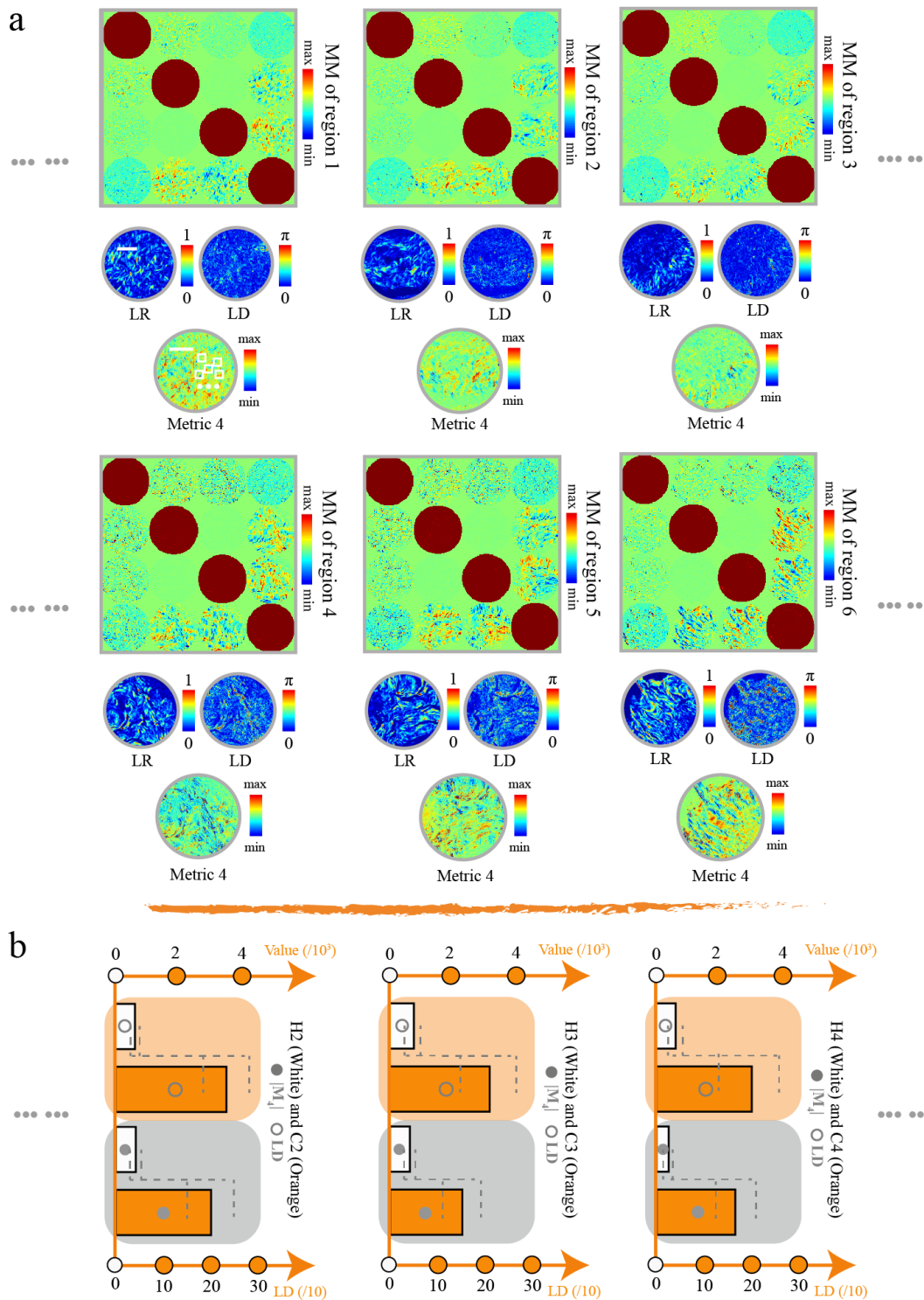
Supplementary Figure S8. Monte Carlo simulation for the optical properties of the waveguides. (a) The model of a linear diattenuator and a depolariser (isotropic and anisotropic scattering induced), as well as a multi-layered retardance geometry. (b) Azimuthal dependence curves of the MM elements for SCBM. All the MM elements are normalized by m_{11} . Cases 1 to 3 consist of different layered structures, as explained in the text.

Supplementary Material 7: Data acquisition, data processing, and statistical analysis for non-small cell lung carcinoma

Lung cancer is one of the most commonly diagnosed cancers, and accounts for more than 20% of all cancer deaths worldwide⁴². Clinically, non-small cell lung carcinoma is the primary form of lung cancer constituting about 85-90% of all lung cancer cases^{43,44}. Fibrous structures of the extracellular matrix play an important role in the development of non-small cell lung carcinoma tissues since they provide strength and cushioning^{45,46}. Recent studies showed that the proportions and distribution of such fibrous structures are different between normal and cancerous lung tissues^{45,46}. These differences can be identified with hematoxylin and eosin (H and E) staining. However, for quantitative and accurate evaluation of detailed structural changes of fibrous structures in non-small cell lung carcinoma tissues, MM microscopic imaging was used in this study. Here we selected five 12- μm -thick non-small cell lung carcinoma tissues slices for demonstration. For pathological comparison, the corresponding 4- μm -thick H and E stained slices were also prepared. The sample selection and preparation were performed by experienced pathologists. The age range of the patients was from thirty to fifty-five years. This work was approved by the Ethics Committee of the Shenzhen Second People's Hospital.

Measurements were taken using a conventional MM microscope and the retardance was derived via MMPD, a method that has been used for cancer differentiation in various works¹¹⁻¹³. We selected 10 points per region; 2 regions were chosen from a sample, one containing normal and one containing cancerous tissue. The statistical analysis followed the approach of Ref²⁶ (Supplementary Figure S9a). The field of view (FOV) of the MM microscope was 0.77 mm² and its calibrated precision was lower than 0.3%. We calculated the mean value and standard deviation of the retardance across the same areas to set as ground truth for comparison with the absolute value of metric 4. Example MMs, as well as corresponding MMPD parameters, M_4 value from healthy or cancerous tissue and quantitative statistic histograms are illustrated in Supplementary Figure S9.

Supplementary Table S2 contains the data measured by two parameters as well as the corresponding P-value, which shows the significant difference between the two classes of samples. Considering the original data distribution and the P-values of either individual samples or the overall combination, it can be found that the metric 4 is able to distinguish efficiently between healthy and cancerous tissue. To make the process more efficient and precise, further detailed error analysis and corresponding optimization will be the subject of further work.



Supplementary Figure S9. Demonstration of original MMs, decomposed parameters, value of metric 4 and statistical histograms of healthy and cancerous lung tissue. (a) MMs and related parameters – alongside with the value of linear diattenuation

(LD), linear retarder (LR), metric 4; Note the scale used for LD, LR, and M_4 has been amplified by a factor of 4, 5 and 20 for better visualisation²⁶. (b) Statistical histograms of some samples (note here we use the absolute value of metric 4). Gray dotted lines represent the standard deviation.

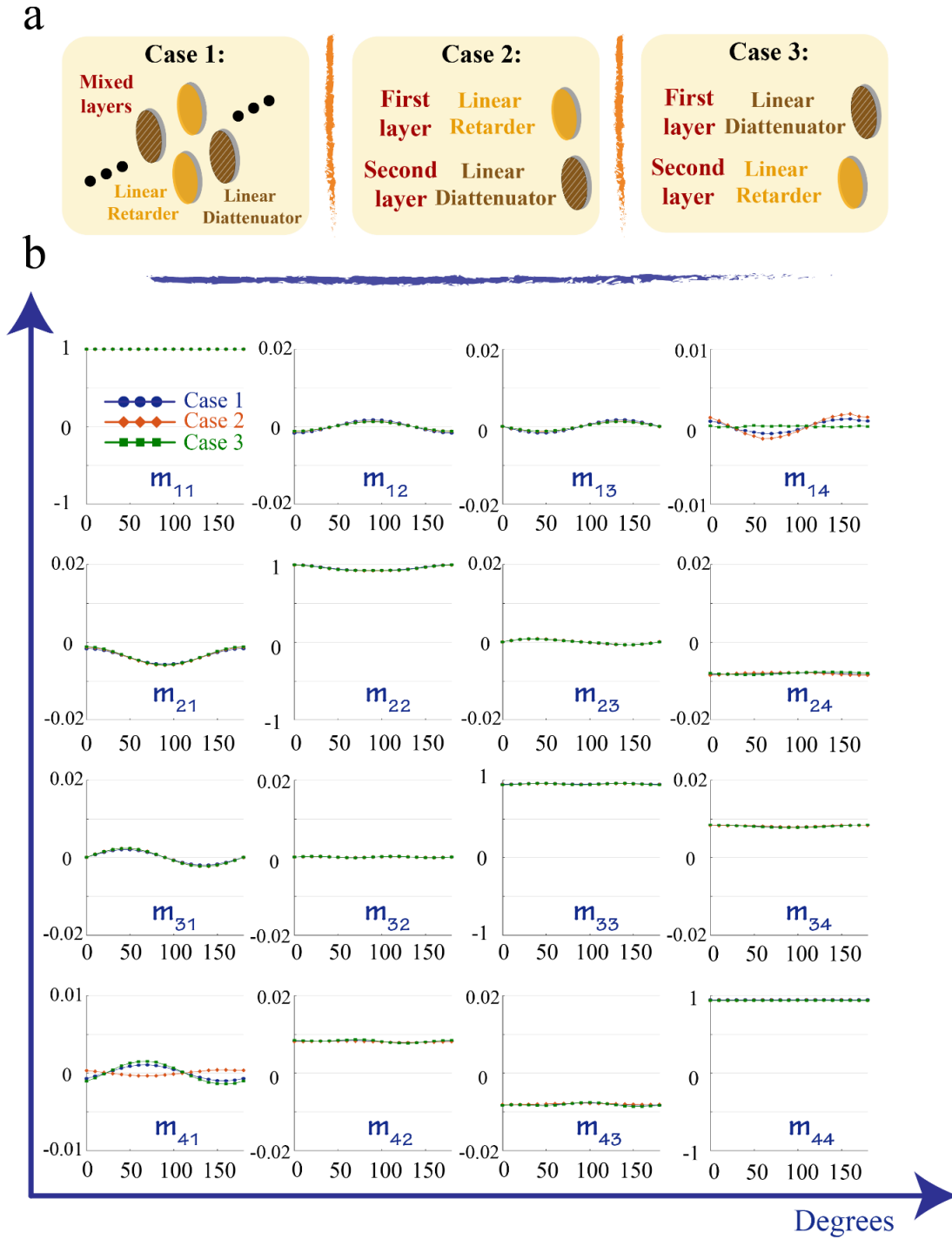
Supplementary Table S2. Value of retardance and metric 4 of the samples used in this work
(Retardance: /10¹; M_4 : /10³)

	Slide 1 (H1 and C1)				P- value	Slide 2 (H2 and C2)				P- value
	Healthy		Cancerous			Healthy		Cancerous		
	mean value	standard deviation	mean value	standard deviation		mean value	standard deviation	mean value	standard deviation	
Retardance	3.78	1.56	16.22	4.23	<0.001	4.51	1.42	19.31	5.02	<0.001
$ M_4 $	0.39	0.21	2.84	0.77	<0.001	0.32	0.09	3.75	0.86	<0.001
	Slide 3 (H3 and C3)				P- value	Slide 4 (H4 and C4)				P- value
	Healthy		Cancerous			Healthy		Cancerous		
	mean value	standard deviation	mean value	standard deviation		mean value	standard deviation	mean value	standard deviation	
Retardance	4.56	1.39	15.73	3.97	<0.001	2.24	0.82	17.55	3.34	<0.001
$ M_4 $	0.42	0.19	3.13	0.89	<0.001	0.24	0.11	2.92	0.93	<0.001
	...				P- value	Combination of all slides				P- value
	Healthy		Cancerous			Healthy		Cancerous		
	mean value	standard deviation	mean value	standard deviation		mean value	standard deviation	mean value	standard deviation	
Retardance	...					3.39	1.15	17.31	4.07	<0.001
$ M_4 $...					0.29	0.13	3.29	0.82	<0.001

Supplementary Material 8: Monte Carlo simulation for double-layered system

As shown in the Fig. 4d in the main article, as well as Supplementary Material 2, the zero or non-zero values of m_{14} or m_{41} represent different layered structural information of tissues. Previous studies have demonstrated that such layered structures exhibit different linear diattenuation and retardance properties^{7,8}, which may be helpful for biomedical measurements. Here, for a better understanding of the experimental results, we carry out MC simulation^{40,41} with a cylinder birefringence model (CBM) to simulate the interactions between polarised light and the fibrous structures of tissues. In the CBM model, the infinitely long cylindrical scatterers can provide similar anisotropic scattering effects and linear diattenuation to that generated by the tissue fibers. During the MC simulations the scattering coefficients, refractive indices, sizes, orientation, angular distribution of the cylindrical scatterers, and the value and fast axis orientation of birefringence for interstitial medium can be adjusted. Here in this study, the simulation parameters were set as follows. For the two-layered medium, the thickness of both layers was 0.006 mm; for the layer consisting of scattering cylinders, the scattering coefficient and size were 200 cm^{-1} and $0.05 \text{ }\mu\text{m}$, respectively; the cylinders were distributed along the X axis direction with 5° fluctuations; for the layer of birefringent medium, the value and fast axis orientation were set to be $\Delta n=0.002$ and 22.5° , respectively.

Supplementary Figure S10a gives three cases that we simulated in this section, which represent different morphologic geometries in such human lung samples. From the simulated results shown in Supplementary Figure S10b we can observe that the m_{14} and m_{41} elements show asymmetric properties, especially for cases 2 and 3, in which the value of m_{14} (or m_{41}) has a more prominent fluctuation than that of the m_{41} (or m_{14}) with the direction change of cylinders. For the medium in case 1 combining cylinders and birefringence in the same layer, this asymmetric property occurs in both elements. Meanwhile, other MM elements of such a two-layered medium are symmetrical.



Supplementary Figure S10: Monte Carlo simulation for the optical properties of a biomedical sample. (a) The model of case 1 (mixed-layered geometry), case 2 (first layer: linear retarder, second layer: linear diattenuator), as well as case 3 (first layer: linear diattenuator, second layer: linear retarder). (b) Azimuthal dependence of the MM elements for CBM. All the MM elements are normalized by m_{11} .

Supplementary Material 9: More vectorial metrics derived from the Mueller matrix

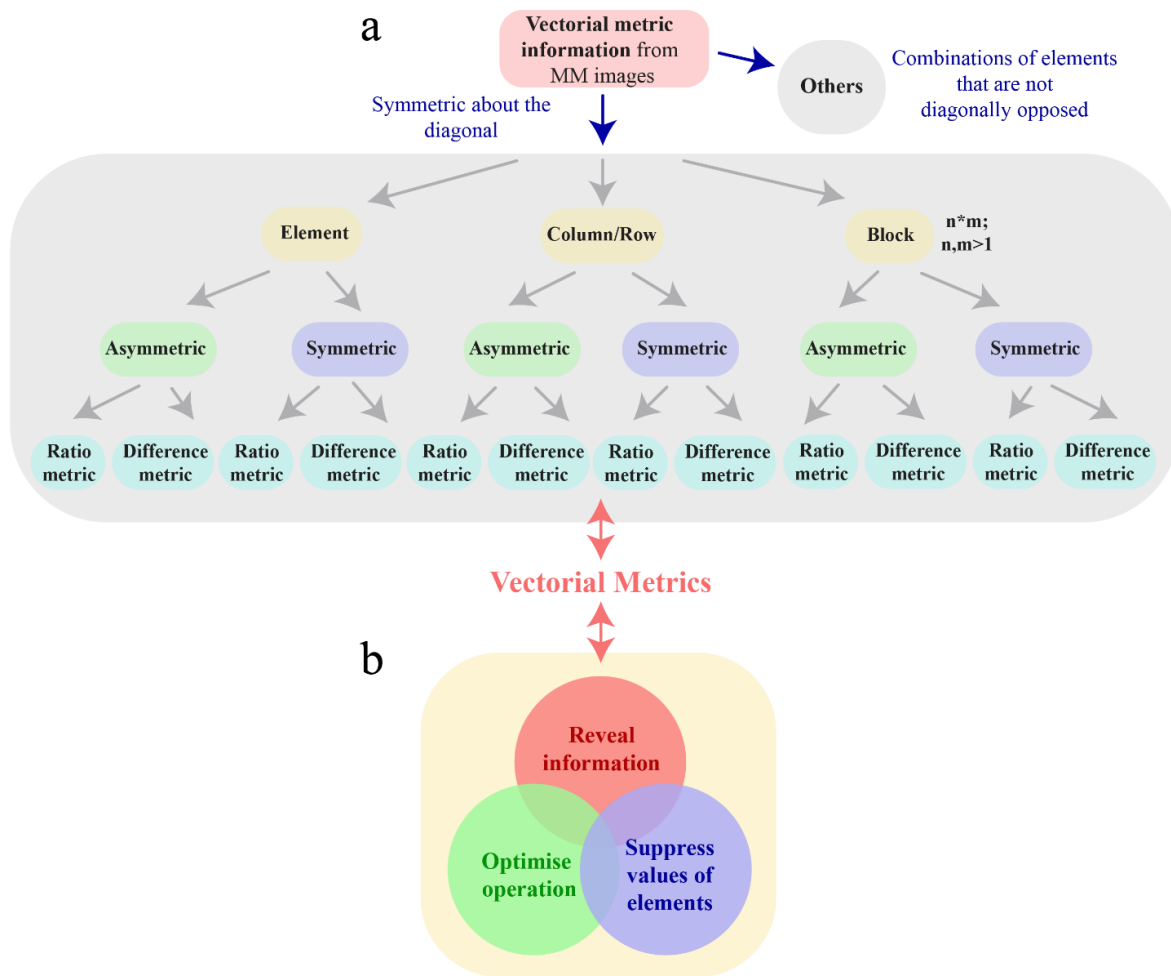
The four previously introduced metrics (1, 2, 3 and 4) are based on analysing the asymmetric or symmetric properties of the MM images; these could be referred to as “difference metrics” that have the form $(X-Y)$, where X and Y are each MM elements (or combination of elements). The new proposed metrics (metric 5 in the discussion) could be defined as a “ratio metric” in the form (X/Y) where X is the MM element (or combination of elements) that can be expected to be near-zero; Y is a reference value derived from the element m_{11} .

Through exploration of various cases, we can categorize the different metrics according to the unified map in the figure (Supplementary Figure S11a). We mainly present three general types of metric in the note: element-wise, column/row-wise and block-wise. Specifically, for block-wise, as the MM is a 4×4 matrix, the sub-block would be an $n \times m$ sub-matrix ($1 < n, m < 4$). Where one metric belongs to above categories. To form a new metric, we may choose any combination of elements; we do not need to be restricted to symmetrically opposed elements (see Supplementary Figure S11a).

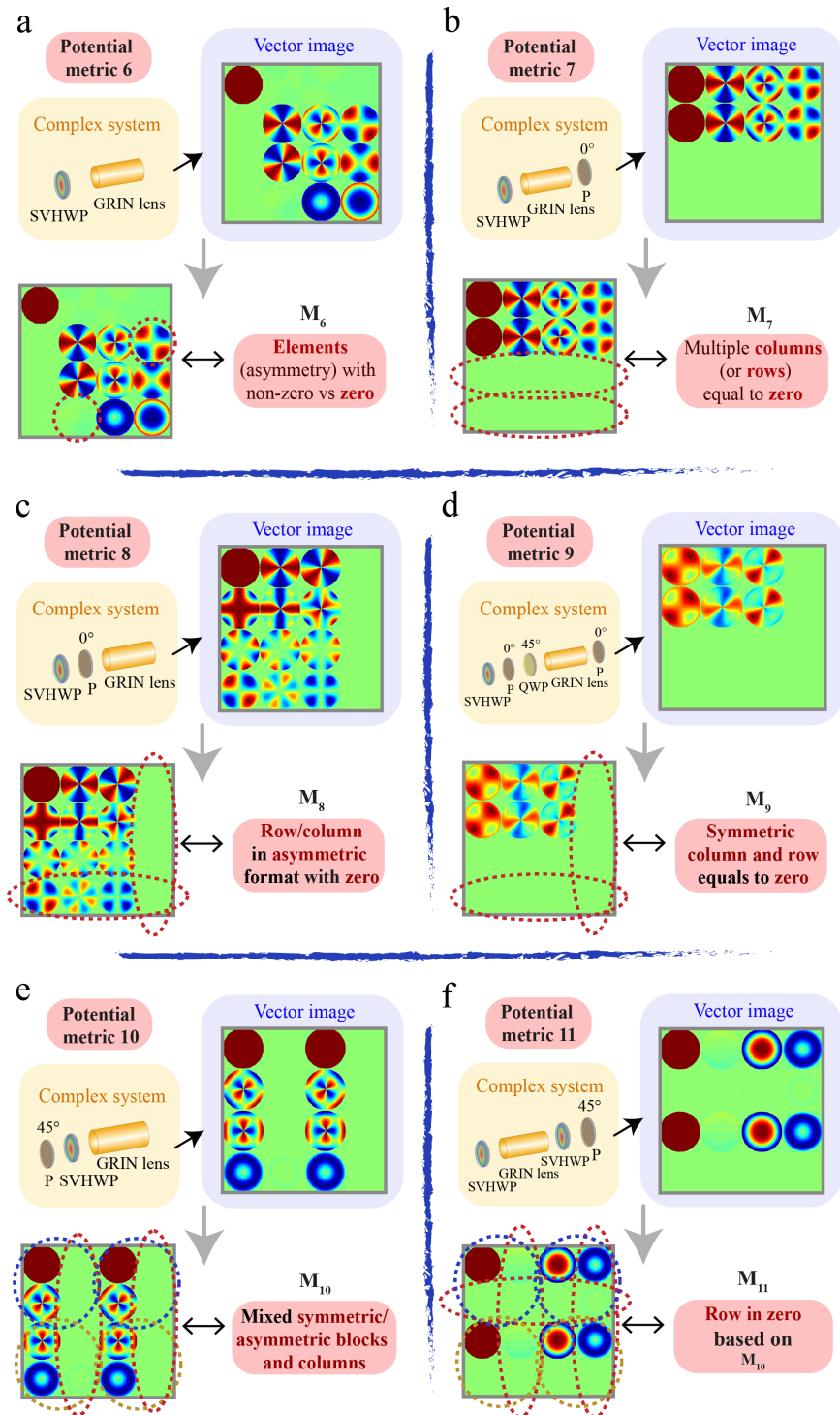
Some new vectorial metrics are defined in Supplementary Figure S12, which additionally reveals six potential metrics (metric 6 to 11) beyond the ones that have been explained in the main article. Supplementary Figure S13 shows two pairs of GRIN lens cascades with theoretical and experimental data as validation examples. These cases have been illustrated using a spatially variant half-wave plate array (SVHWP) based GRIN lens cascade²⁴; their MMs and certain vectorial properties are shown in Supplementary Figure S14. Here we provide just a brief illustration of the possibilities for other metrics that can be further developed within the scope of Supplementary Figure S11a.

We then give a brief summary in Supplementary Figure S11b about the functionalities of the vectorial metrics that appeared in this paper. They can act as indicators to 1) reveal information of complex optical systems (e.g., metric 1-5); 2) optimize operation such as a feedback metric for control purposes (e.g., metric 2, 3 and 5); 3) suppress values in the MM (e.g., metric 6 to 11, maintain various elements whose absolute values have been suppressed). The third

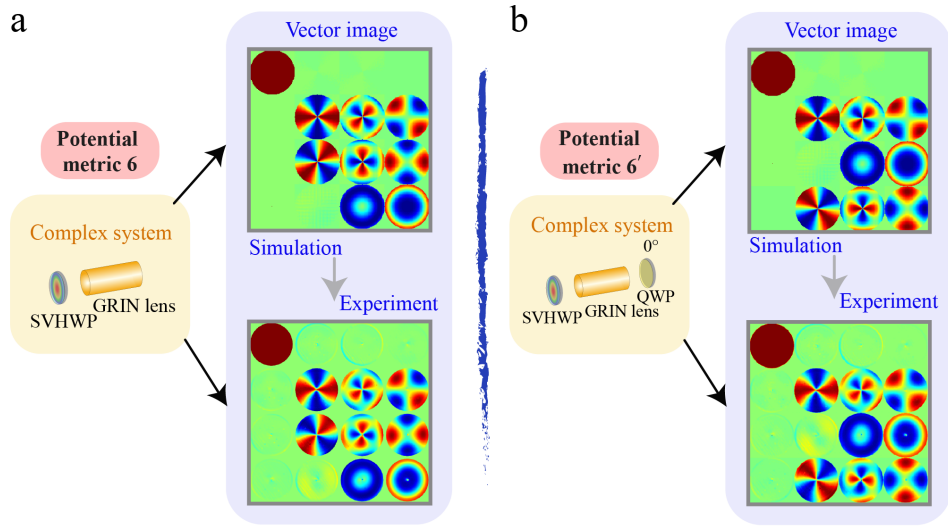
functionality, which is revealed here, may provide an intriguing possibility to edit the presence of a particular physical property, or do vectorial coding/decoding of the MM itself via its sixteen elements. The overall picture shows the opportunity for further investigation of such vectorial metrics.



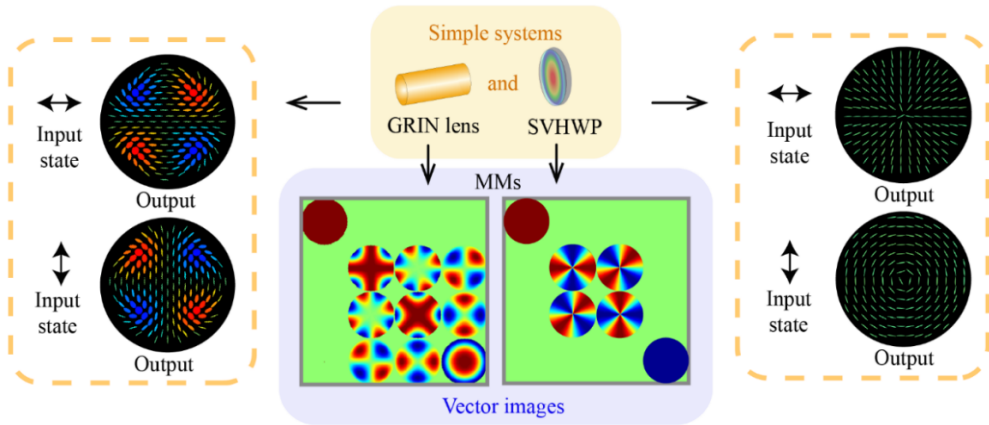
Supplementary Figure S11. Vectorial metric information from MM images. (a) The picture gives an overview of different categories of the information extraction from the MM vector images. (b) Three characteristics of the vectorial metrics.



Supplementary Figure S12. Six additional proposed metrics. For metrics 6 to 11, they are illustrated using MMs of different GRIN lens cascades. The metrics belong to the different types mentioned in Supplementary Figure S11. All MMs are normalized as a ratio to m_{11} .



Supplementary Figure S13. Validations between simulated and experimental MM data. Sketches of (a) proposed metric 6 and (b) its modified format (proposed metric 6'; which belongs to "ratio metric" with zero-valued one element) show the corresponding GRIN lens cascades. Simulations and experimental MM data are presented.



Supplementary Figure S14. MMs and generated vector beams of GRIN lens and SVHWP. MMs and vector beams generated via GRIN lens and SVHWP are given, the input polarisation states are also shown in the figure.